International Journal of Thermal Sciences 181 (2022) 107782

Contents lists available at ScienceDirect

International Journal of Thermal Sciences

journal homepage: www.elsevier.com/locate/ijts

A biomimetic design of steam turbine blade to improve aerodynamic performance

Fan Wu, An Han, Wei Jiang **, Yanan Yue ***, Danmei Xie *

Key Laboratory of Hydraulic Machinery Transients (MOE),Wuhan University, Wuhan, Hubei, China

A B S T R A C T

The complex flow field at low load will affect the aerodynamic performance of steam turbine. To improve the performance in low mass-flow condition, we proposed a design of bio-inspired steam turbine blade with biomimetic bumps on suction side. We built a series of biomimetic blades based on a last stage rotor blade of nuclear low-pressure to analyze the function of the bump. The numerical simulation results declared that bumps generated streamwise vortices. There existed a region with low-pressure on suction side which was suitable for vortices to be generated and to develop. Under the influence of streamwise vortex, the steam flow near suction side was restricted in a low velocity. The energy exchange between blade and the main flow was blocked. The pressure on suction side decreased. Therefore, the performance of blade was improved, reflecting in the raised output torque. The output torque of optimum biomimetic blade raised from a negative value −26.31 N m to a positive value 2.13 N m in low mass-flow condition. To explore the function of bump, we also built a blade with vortex generators at the same place. The result shows that the bumps on blade cause less pressure loss for the turbine passage and the vortices generated by them influenced wider region in the flow field. The current work provided a new design route for modifying turbine rotor by flow control structure.

1. Introduction

Although the proportion of renewable energy is keeping increased in the electricity grids, most of global electricity is generated by the steam turbines at present. As the solar and wind power stations are not available to regulate the load on grids frequently, there is a growing need for the steam turbine to undertake the task of peak-load regulation. When the peak-load on grids decreases, the steam turbine typically operates in an off-rated condition, in which the mass-flow rate of steam is much lower than that in the rated condition. The work capacity of turbine blade is reduced with the decreasing mass flow rate, which also degrades the system efficiency and safety. Therefore, it is necessary to develop an advanced blade to enhance the aerodynamic performance and energy efficiency of steam turbine, especially in the working conditions of low mass flow rate.

Recently, many works were conducted on the structure optimization of either airfoil [1] or steam turbine blade [2,3] for better performance. The way by imitating living animals, such as dolphin [4], bird [1], humpback whale [5] and so on, was proved to be effective on airfoil. The pectoral flipper of humpback whale (Fig. 1) provides scientists a novel strategy to improve the aerodynamic performance of foils [6]. When the humpback whale swims in the ocean, the bumps at leading edge of the whale flippers can generate many streamwise vortices, increase the lifting force on the flippers, and accelerate the movement of whale [7–9]. Inspired by the unique structural topography of bumpy structures on the whale flippers, various foil of aircrafts and blade of turbomachines with bumps have been developed in past few years such as, airfoils [10], fans [11], wind turbines [12,13], and tidal turbines [14]. Recent studies reveal that the bumps patterned at the leading edge of airfoils form an adverse pressure gradient on the suction surface and generated the vortex pairs between the bumpy structures [15]. The amplitude and wavelength of bumps dominate the vorticity and lifting capability of airfoils [16,17]. With a rational design of the bumps, the generated vortices effectively force the flow direction to change and suppress the flow separation on the foils [18–20]. Therefore, the bumpy leading edge can provide sufficient lift even when the angle-of-attack (AOA) is less than the stall AOA for the conventional smooth foils [21, 22]. However, the bumpy structures may decrease the lift coefficient of airfoils, depending on the Reynolds number and AOA. In the flow filed with high Reynolds number, the bumpy leading edge would induce a flow separation behind the bumps [23]. When the AOA increases, this separation region would move forward and reduce the lift of airfoil. By contrast, the smooth airfoils can generate a higher lift force in the condition of large AOA, because the air flow behind the smooth leading

* Corresponding author.
** Corresponding author.
*** Corresponding author.
E-mail addresses: jiangwei@whu.edu.cn (W. Jiang), yyue@whu.edu.cn (Y. Yue), dmxie@whu.edu.cn (D. Xie).

https://doi.org/10.1016/j.ijthermalsci.2022.107782
Received 17 January 2022; Received in revised form 26 April 2022; Accepted 28 June 2022
Available online 6 July 2022

edge is more stable [24]. In steam turbine blade, the bump on leading edge of linear blade can raise the output torque in off-rated condition [25].

For the steam turbine, it is more difficult to develop a biomimetic blade with enhanced aerodynamic performance because the flow field in turbomachinery is complicated. In contrast to the airfoils, the steam turbine blades are usually twisted with differing section profiles. The air flowing around the airfoils has no apparent boundary but the steam flowing through the turbine blades is constrained in the cylinder. Thus, the turbulent flow in steam turbine has a significantly large radial velocity with the varying AOA along the radial direction, making the bumpy leading edge failed to generate streamwise vortices and enhance the lift. Despite intensive effort, it remains challenging to design a blade that can improve the aerodynamic performance of steam turbine in such complicated flow field. In this work, to enhance the aerodynamic performance, we designed a novel biomimetic blade on which the bumpy structures were mounted on the suction surface. We conducted a systematical numerical simulation to investigate the aerodynamics on the turbine blade and optimize the bumpy structural topography. Compared with the original design, the biomimetic blade with bumpy suction surface generated streamwise vortices behind the bumps. The biomimetic blade increased the output power (measured by the output torque) by decreasing the applied steam pressure on the suction surface. Especially for the low mass flow rate of steam (40% of the rated value), the new biomimetic blade can increase the output torque (τ) from negative (−26.31 N m) to positive (2.13 N m). The generated vortices prevented the kinetic energy exchange between the suction surface and the main flow. Moreover, the vortices avoided a high-pressure loss for disturbing the original flow field. In contrast to the traditional strategy using the vortex generator (VG) on blade, the well-designed bumpy structures reduced ~40% of pressure loss for the steam flow, while resulting in ~20% higher output torque on the blade. Our work not only expands the knowledge boundaries of turbomachinery design, but also provides a new avenue to promote the energy performance for various industrial applications.

2. Numerical methods and validation

The new biomimetic design of turbine blade was developed based on the rotating blade at last stage in the low-pressure cylinder of a nuclear steam turbine. Fig. 2 shows the physical model of the biomimetic rotating blade with geometrical parameters. The height (l_0) and the axial chord length (C_l) of the original turbine blade are 1828 mm and 557.7 mm, respectively. The bumpy structures were mounted on the suction surface of turbine blade. In this study, five geometrical parameters of bumps, including the amplitude (A), number of bumps (N), upstream width (W_U), downstream width (W_D) and deflection angle (δ) were adjusted to enhance the aerodynamic performance of turbine blade.

To study the effects of bumps on the flow field and output torque for the turbine blade, we established the computational fluid dynamics calculation domain for a stator blade and a rotating blade, as shown in Fig. 3. The ANSYS-CFX was employed to simulate the flow field. The Euler-Euler coordinate system was adopted for the numerical calculation. The equilibrium phase change model was used with the assumption of local thermodynamic equilibrium for the mixture of two phases in steam. The lever rule was used in the flow solver, and thus the mass fraction of the vapor (χ) is defined as

$$\chi = \frac{h_{mix} - h_{sat,l}(p)}{h_{sat,v}(p) - h_{sat,l}(p)} \tag{1}$$

where h_{mix} is the mixture static enthalpy, $h_{sat,l}(p)$ and $h_{sat,v}(p)$ are the saturation enthalpy of liquid and vapor, respectively. When $0 \le \chi \le 1$, the mixture contains liquid and vapor. The thermophysical properties of liquid-vapor mixture can be calculated using the lever rule by using the mass fraction of vapor and the properties of saturated liquid and vapor, which was given by

$$\psi_{mix}(p) = (1-\chi)*\psi_{sat,l}(p) + \chi * \psi_{sat,v}(p) \tag{2}$$

whereψ denotes the thermophysical property of fluid, such as entropy, enthalpy, specific heat, thermal conductivity or dynamic viscosity.

The density of liquid-vapor mixture in the saturated condition is calculated using the harmonic averaging,

$$\frac{1}{\rho_{mix}} = \frac{1-\chi}{\rho_{sat,l}} + \frac{\chi}{\rho_{sat,v}} \tag{3}$$

where ρ_{mix} is the density of liquid-vapor mixture, $\rho_{sat,l}$ is the density of saturated liquid, and $\rho_{sat,v}$ is the density of saturated vapor. The properties of saturated liquid and vapor were obtained from the IAPWS IF97 material library. To ensure the accurate simulation of boundary layer that capture flow separation near the blade surface, we employed the inflation mesh with the first layer thickness of 0.01 mm and 16 layers of growth mesh.

The k-omega SST model was used in the numerical simulation due to the advantage on predicting the flow separation under adverse pressure gradient. The k-omega SST model is a widely selected model to predict flow separation, such as in the stall operation of airfoil (ideal gas condition) [26], and in the windage of steam turbine blade (steam condition) [27–29]. Fig. 4 shows the axial velocity from CFD simulation and experiment after the last stage rotor blade [29]. The experiment was conducted in a two stages steam turbine model. In Fig. 4, the negative axial velocity represented the reverse region in flowfield. This result shows that the k-omega SST model can predict reverse region accurately, which was of importance in prediction of flow separation.

To validate the accuracy of numerical model, we also simulated the condensing steam flow in a three-dimensional linear blade cascade, in which the blade geometry and boundary conditions were same as the

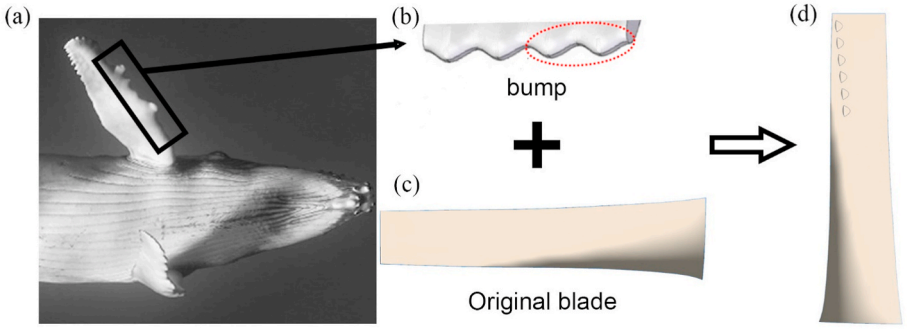

Fig. 1. The inspiration of biomimetic blade. (a) Humpback whale with bumpy flippers. (b) Bumps designed by imitating the flippers of humpback whale. (c) Original blade. (d) Biomimetic blade. We set the bumps on a steam turbine blade. Note that the bumps can not only set at the leading edge, but at somewhere near the leading edge.

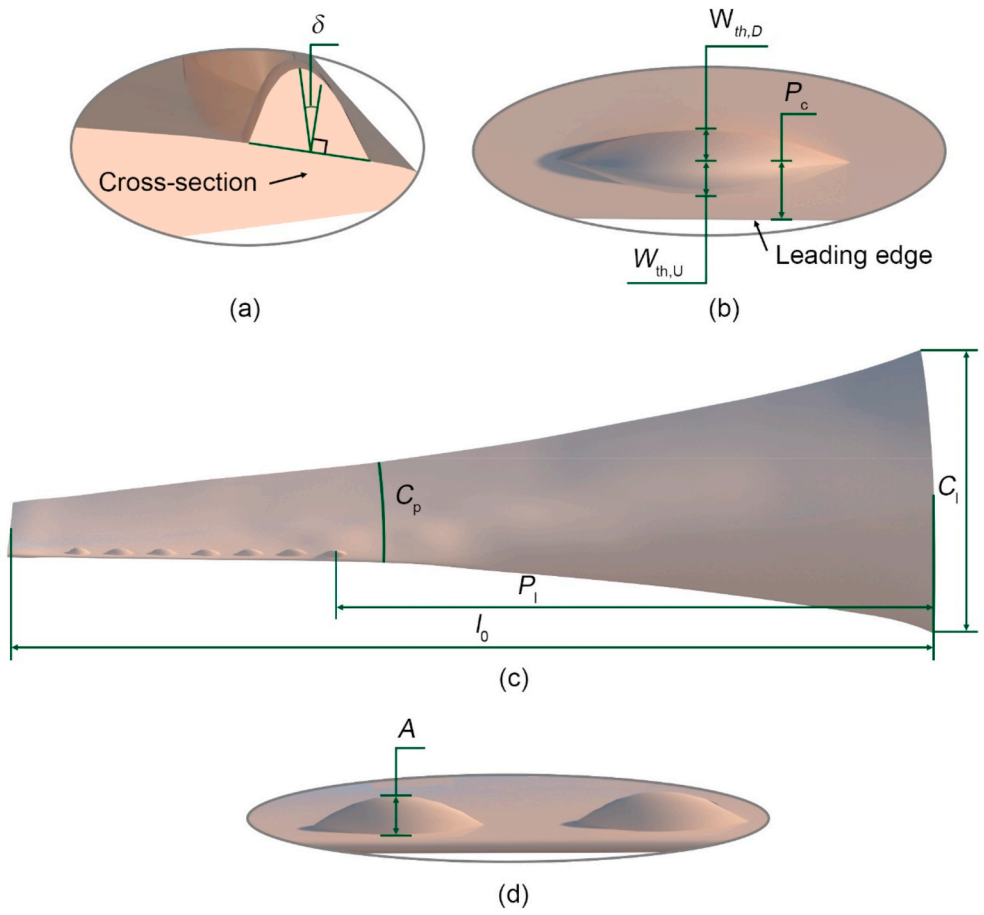

Fig. 2. The parameters of biomimetic blade. (a) δ presented deflection angle of bumps and a negative/positive value meant the angle deflect toward the trailing edge/leading edge. (b) According to the direction of steam flow, the bump was controlled by the upstream width (W_U) and the downstream width (W_D). P_c presented bump position in chordwise. (c) Blade height l_0 equals 1828 mm and axial chord length C_l equals 557.7 mm. P_l presented bump position in radialwise. C_p presented the length of suction side profile. (d) The amplitude A controlled the distance from the bottom to the tip of bump.

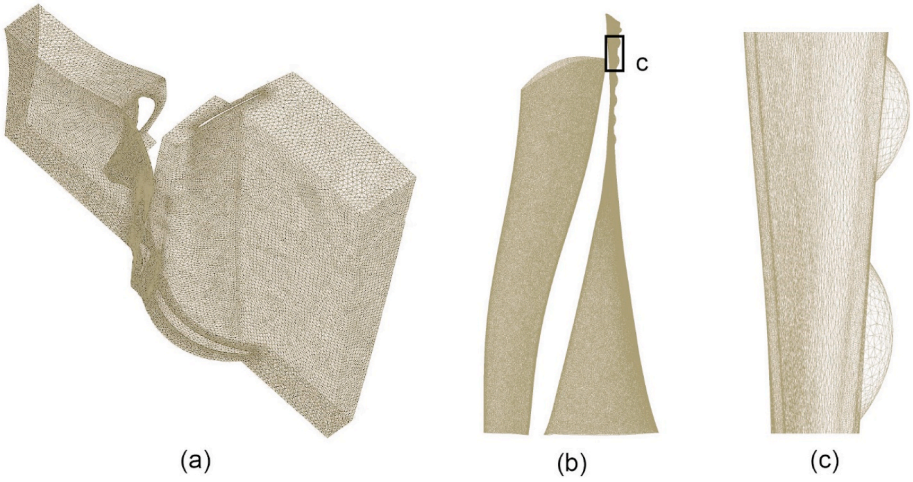

Fig. 3. Calculation domain contains a stator blade and a rotating blade. (a) Mesh of steam domain. (b) Mesh of blade surface. (c) Local mesh around the bumps.

experiment in literature [30]. In the validation case, the total pressure and temperature of steam at the inlet were 89 kPa and 373.13 K, respectively. The mean static back pressure of steam at the outlet was 39 kPa. Fig. 5 compares the simulated steam pressure distribution on the linear blade with the experimental measurements in the literature. The simulation result agrees well with experiment data, especially for capturing the pressure variation near the trailing edge. The average error between the simulation results and experiment data was 5.82%, which confirmed that our numerical method provides a reliable prediction for the steam condensation in steam turbine. Table 1 summarizes the results of output torque τ for the simulation cases with different mesh density. The output torque τ is constructed by,

$$\tau = \left(\int_S (\vec{r} \times (\hat{\tau} \bullet \vec{n}))dS \right) \bullet \vec{z} \tag{4}$$

where S is the blade surface, $\hat{\tau}$ is the stress tensor on a micro-surface of blade, $\vec{n}$ is the unit normal vector of the micro-surface, $\vec{r}$ is the position vector, $\vec{z}$ is the unit vector of axis.

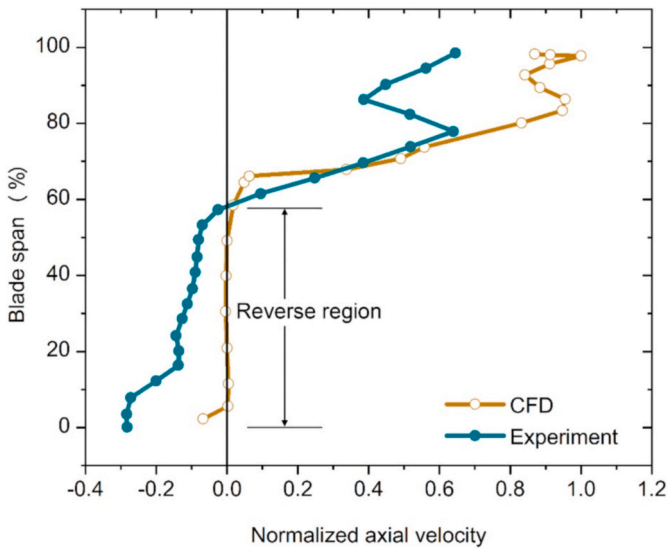

Fig. 4. Comparison of axial velocity distribution along blade spanwise in the outlet of rotor.

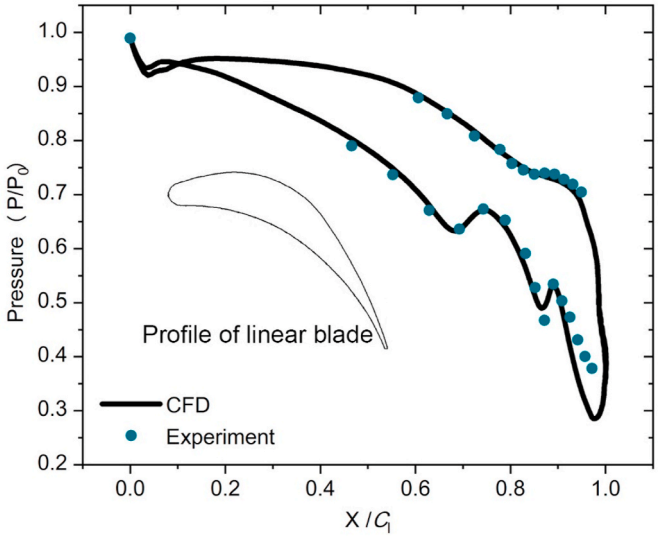

Fig. 5. Validation linear blade profile and numerical simulation result.

Table 1
Mesh independence validation.

Case	M1	M2	M3	M4
Nodes	1325270	2595782	3263036	4433861
τ/N•m	2650.70	2644.48	2643.97	2643.53

Case M2 to Case M4 have very close values of the τ (~0.04%). This indicated that more nodes than case M2 in the mesh do not change the calculation accuracy. The best compromise between computational time and quality results was probably represented by the CFD calculation carried out with 2.6 million nodes (case M2).

In this work, we simulated the flow field of the turbine passage with biomimetic blade and original blade in two operating conditions, the rated condition with steam mass flow rate of 2.9 kg s^{-1} (G_0) and the off-rated condition with $0.4G_0$. For the rated operating state, the boundary conditions at the inlet (before stator blade) were set with the mass flow rate of 2.9 kg s^{-1}, the mass fraction of vapor of 0.88 and total temperature of 329.77 K, respectively. At the outlet (after rotating blade), the static pressure was set as 5400 Pa. For the operating condition with $0.4G_0$, in which the mass flow rate was 1.16 kg s^{-1}, the mass fraction of vapor was 0.87, the total temperature at inlet was 332.98 K, and the average static pressure at outlet was 5400 Pa.

3. Results and discussion

3.1. Design of bump position on the suction side

For the rotating blade at last stage of steam turbine, AOA was near 0° in most operation conditions, which greatly suppress the enhanced aerodynamic performance by bumps on the leading edge. We explored the suitable design of bumps for turbine blade by analyzing the flow field of original blade. Fig. 6 (a) shows the streamline of steam flow near the twisted rotating blade in $0.4G_0$. With the steam flow rate decreasing, a backflow appeared from the root of blade and the steam flows toward the tip. As the turbine blade rotated in the speed of 1500 rpm, the steam had a large radial velocity and the steam density kept raising when the steam flow got close to the tip of blade. For strengthening the turbulence generation, the bumps should be positioned on the blade portion of 65% l_0 to 100% l_0 (denoted by the density of streamline in Fig. 6a), where the steam density was higher than that at the root of blade. As denoted by the black circle in Fig. 6 (b), in the condition of $0.4G_0$, a low-pressure region existed at the high curvature part of the blade profile, which was the throat of the rotor passage. As the steam expanded at the throat, the pressure dropped and the steam velocity increased so a low-pressure region appeared. Meanwhile, with the steam expanding, the velocity direction of steam varied, guaranteeing an AOA for the bumps to generate vortices effectively.

The effects of bump position on turbulence generation were investigated by comparing the flow fields of two types of bumpy blades (named B_1 and B_2), as shown in Fig. 7a & b. We fixed the shape but changed the position of bumps. For blade B_1, the bumps were set at intervals along the leading edge. For blade B_2, the bumps were positioned at the low-pressure region on the suction side. The amplitude A of bumps was fixed at 1.8% of the axial chord length C_l. Both of the upstream width W_U and downstream width W_D were 2% of the profile length of suction side C_P. The deflection angle δ of bumps was set at 0. The number of bumps N on blade B_1 and B_2 was 7 and 6, respectively. The last bump near the root of blade B_2 was removed because it is far away from the leading edge and contribute little to the vortex generation. Table 2 shows the position of bumps on the blade B_1 and B_2.

Fig. 7 (a) and (b) demonstrated the streamlines on two blade surfaces obtained from the numerical simulation. The streamlines developed clockwise and formed the single streamwise vortex behind each bump, which was distinct from the generation of vortex pairs on the airfoils. This unique phenomenon is attributed to the suppression of counter-clockwise vortex by the large radial velocity of steam flow in turbine. The simulation results revealed that the average steam velocity in streamwise direction was 37.8 m/s, but the average velocity in radial direction reached 43.6 m/s. As the counterclockwise vortex in the vortex pairs was opposite to the direction of radial steam flow, it would be suppressed and rapidly dissipated, leaving single clockwise vortex behind the bumpy structures. The streamlines shown in Fig. 7 (a) also indicated that the clockwise vortices on B_1 surface dissipated at the low-pressure region on the blade surface, where the curvature of blade profile was high (i.e., throat of rotor passage). As the direction of steam flow was forced to change at the throat of rotor passage, the circumferential component of steam velocity varied sharply. Because the streamwise vortex was the result of the velocity gradient in both radial and circumferential directions, the large variation in the steam flow direction break the vortex stability. As a consequence, the clockwise vortices on B_1 surface cannot pass the low-pressure region and just affected a small area at the upstream portion of rotor passage.

By contrast, when the bumps was set along the low-pressure region on surface, as shown in blade B_2, the change of steam direction has no

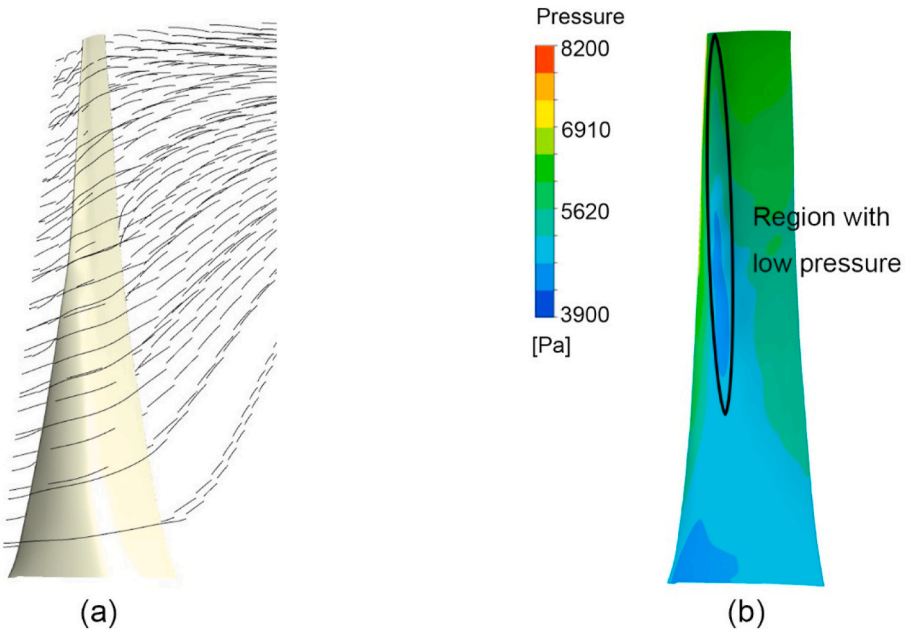

Fig. 6. Flow characteristic of original blade in 0.4G0 condition. (a) Streamline in rotating blade area showed an obvious trend to flow toward the tip and the root region was lack of steam. (b) Pressure contour on the suction side of rotating blade. There existed a region with low pressure near the leading edge on suction side.

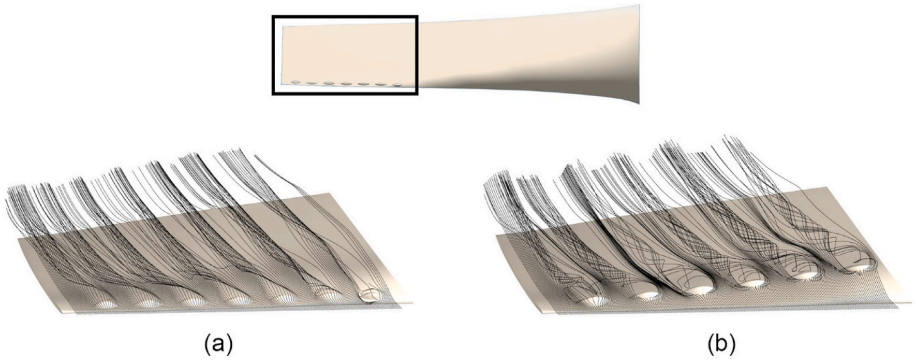

Fig. 7. 3D streamline of two biomimetic blades. (a) The first type of blade (B1) has a row of suction side bumps close to leading edge so the widths of bumps are small. With the influence of radial velocity, the vortices become stable in a certain distance away from bumps. (b) The second type (B2) has the bumps moved to the location where the curvature of blade profile is relative high. The vortices become stable right after the bumps. In this position, the influence of radial velocity are suppressed.

Table 2
The position of bumps defined by center point (start from tip).

B_1	P_c	4% C_P	4% C_P	4% C_P	4% C_p	4% C_p	4% C_p	4% C_p
	P_l	92.5% l_0	88% l_0	83.5% l_0	79% l_0	74.5% l_0	70% l_0	65.5% l_0
B_2	P_c	7%C_p	10% C_p	13% C_p	15% C_p	18% C_p	21% C_p	–
	P_l	92.5% l_0	88% l_0	83.5% l_0	79% l_0	74.5% l_0	70% l_0	–

significant effect on the development of the clockwise vortices. Fig. 7 (b) shows that the streamwise vortices on B_2 surface remained the clockwise rotation till the trailing edge of blade due to the smooth downstream surface behind the low-pressure region. Moreover, the vortices generated by bumps on B_2 surface showed a much stronger vorticity as compared to those on B_1 surface, which effectively reduced the negative output torque τ applied on the blade. For the single rotating blade, the τ on blade B_2 was −15.99 N m, which was 38.9% higher than that on the original blade (−26.18 N m) and 19.2% more than that on blade B_1 (−19.78 N m).

The enhanced output torque of bumpy blade can be attributed to the low-pressure area induced by the vortices behind the bumps on the suction side, as indicated in Fig. 8a & b. However, the bumps also blocked a part of steam flow when generating the vortex. It created a high-pressure area on their upstream surface and decreased the output torque, particularly near the leading edge of blade. As the steam density increased along the radial direction of blade, the bumps close to the tip created the higher pressure on the upstream surface for blade B_1. As comparison, the upstream high-pressure region on blade B_2 was weakened due to the larger spacing between bumps and leading edge (Fig. 8b). The vorticity on blade B_2 was apparently stronger than that on blade B_1, which can be reflected by the wider distribution of lower-pressure area behind the bumps. Because the vortices generated by the bumps on suction side were spaced at intervals, the high vorticity resulted in a clear bumpy edge of the pressure gradient, as denoted by the black curve in Fig. 8b. The pressure contour on blade B_2 demonstrated that the strong vortices can be generated without significant steam blocking, by positioning the bumps along the low-pressure region

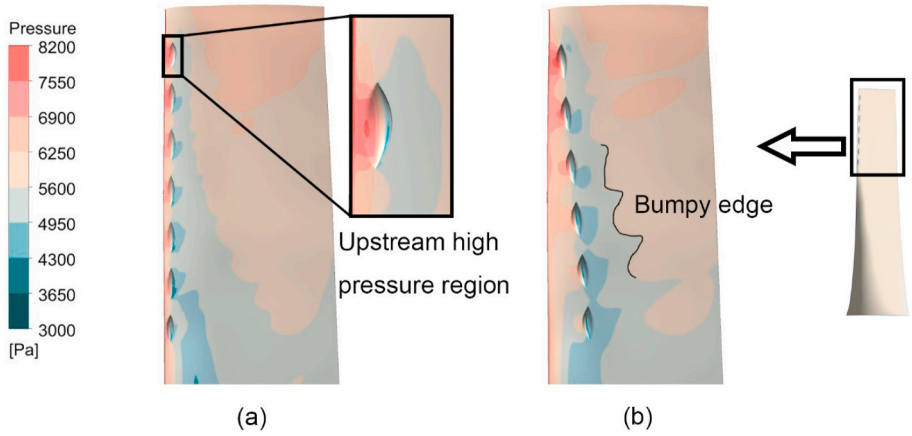

Fig. 8. (a) The pressure distribution of B1. The bumps near leading edge will let its upstream side bear high pressure. (b) The pressure distribution of B2. The pressure on upstream side of bumps decreased with bumps moving away from the leading edge. The bumps of B2 generated stronger vortices, which made an obvious pressure layer on the bumpy edge.

on the suction side of blade. The results explained the higher output torque on blade B_2.

3.2. Geometrical optimization of bumpy structure

To achieve the largest output torque τ on the biomimetic blade, we further optimized the shape of bumpy structures by adjusting the geometric parameters, including the amplitude A, number of bumps N, upstream length W_U, downstream length W_D and deflection angle δ. Fig. 9 presents the process in this section. To be specific, A, W_U and W_D determined the height, upstream and downstream surface profiles of the bumps, respectively. N determined the spacing between bumps. δ controlled the AOA of the biomimetic bumps on the suction side of blade. The orthogonal design was employed in this work to test the comparative effectiveness of the five geometric parameters for the bumpy structures, which allowed us to obtain the optimal design without analyzing massive cases. We defined four levels for the each parameter, as summarized in Table 3.

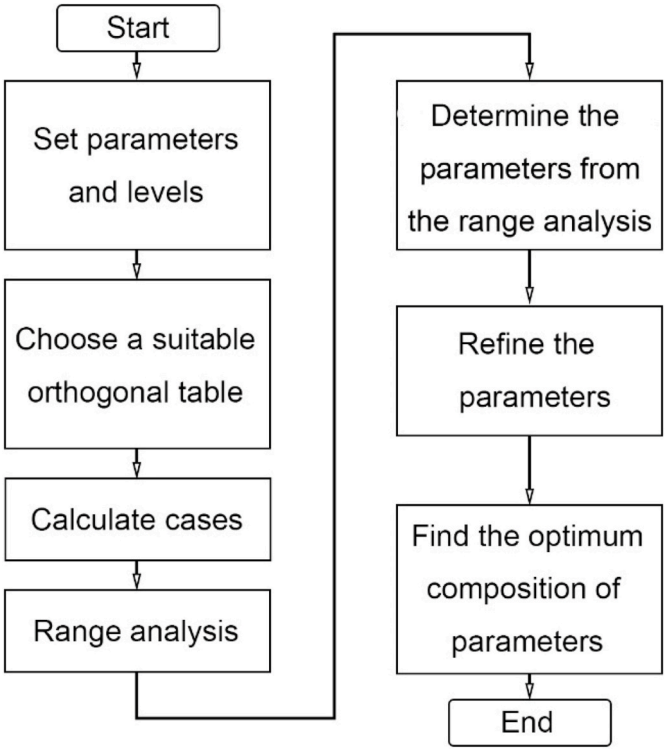

Fig. 9. The flow chart of geometrical optimization.

Based on the guideline of orthogonal design, 16 cases with different bump design (i.e., C1 to C16) was arranged to carry out the simulation. Table 4 shows the orthogonal array of five parameters and the corresponding results of output torque. To analyze the effect of geometric parameters, we fixed one parameter at same level and compared the average output torque ($\overline{\tau}$) for all cases. For example, $\overline{\tau}$ of N at level 1 was the average value of τ for the case C1, C5, C9 and C13. This method is termed as range analysis and the results of $\overline{\tau}$ for each parameter at different level were listed in Table 5.

Fig. 10 shows the variation of $\overline{\tau}$ at different levels of geometrical parameters. Because $\overline{\tau}$ of the biomimetic blade showed a peak value with the increasing level of δ, W_D and W_U, the optimum value of δ, W_D and W_U was determined as 0°, 5% C_P and 4% C_P, respectively. Note that the optimum level of A cannot be directly obtained from the range analysis as $\overline{\tau}$ was proportional to the level of A. We chose level 4 of A as the tentative case for the further optimization. For the range analysis of N, $\overline{\tau}$ on the blade with 6 bumps (level 2) and 10 bumps (level 4) were close. However, from the practical perspective, less modification of the turbine blade was more preferred. Thus, $N = 6$ was selected as the optimal value. Based on above analyses, the parameters of bumps was defined as A = 2.8% C_l, W_U = 4% C_P, W_D = 5% C_P, $\delta = 0°$ and $N = 6$.

During the optimization process, we noticed that the output torque in rated condition was sensitive to the change of A. Different from other parameters, A with big value caused the bumps affected the main flow seriously in the passage, because the bumps with high amplitude took up the space in passage. To further optimize the amplitude A of the bumpy structure, a characteristic parameter R_A was developed to evaluate the overall performance of biomimetic turbine blade under different mass flow rate of steam. R_A is given by,

$$R_A = \varphi_{G_0} \bullet R_{G_0} + \varphi_{0.4G_0} \bullet R_{0.4G_0} \tag{5}$$

where R_{G_0} is the ramp of output torque in the rated condition, $R_{0.4G_0}$ is the ramp of output torque in the off-rated condition ($0.4G_0$), φ_{G_0} is the

Table 3
Parameters and levels for the orthogonal design.

Levels	A (% C_l)	N (number)	W_U (% l_P)	W_D (% l_P)	δ (degree)
1	0.7	4	2	2	−60
2	1.4	6	3	5	−40
3	2.1	8	4	8	0
4	2.8	10	5	11	40

Table 4
Orthogonal table with simulation results of output torque.

Cases	A (% C_l)	N (numbers)	W_U (% l_P)	W_D (% l_P)	δ[a] (degrees)	τ (N•m)
C1	1	1	1	1	1	−23.42
C2	1	2	2	2	2	−16.07
C3	1	3	3	3	3	−23.68
C4	1	4	4	4	4	−23.09
C5	2	1	2	3	4	−19.75
C6	2	2	1	2	3	−19.88
C7	2	3	4	1	2	−22.26
C8	2	4	3	2	1	−17.54
C9	3	1	3	4	2	−19.27
C10	3	2	4	3	1	−21.7
C11	3	3	1	2	3	−14.22
C12	3	4	2	1	3	−11.32
C13	4	1	4	2	3	−9.59
C14	4	2	3	1	4	−10.12
C15	4	3	2	4	1	−23.06
C16	4	4	1	3	2	−16.29

[a] For the parameter δ, a negative value means the angle deflect toward the trailing edge and a positive value means the angle deflect toward the leading edge.

Table 5
Range analysis.

Parameter	$\bar{\tau}$ of Level 1 (N m)	$\bar{\tau}$ of Level 2 (N m)	$\bar{\tau}$ of Level 3 (N m)	$\bar{\tau}$ of Level 4 (N m)
A	−21.57	−19.86	−16.63	−14.77
N	−18.01	−16.94	−20.81	−17.06
W_U	−18.45	−17.55	−10.12	−19.16
W_D	−16.78	−14.36	−18.68	−21.33
Δ	−20.00	−18.47	−16.12	−16.80

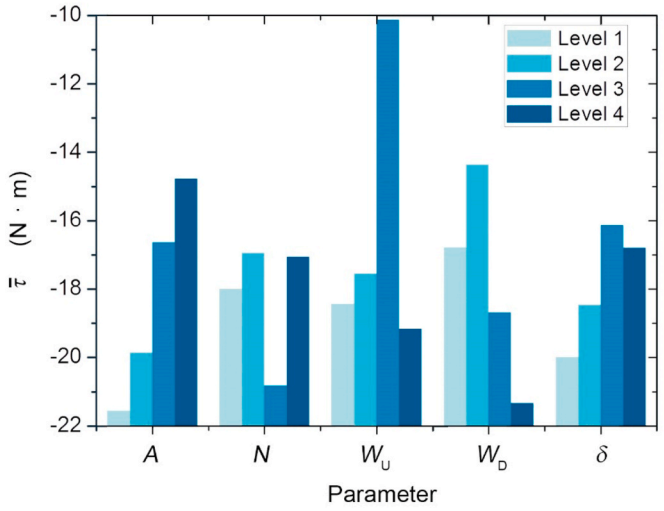

Fig. 10. The variation of $\bar{\tau}$ against the various extraction parameters.

time coefficient for the rated condition in a cycle, $\varphi_{0.4G_0}$ is the time coefficient for the off-rated condition in a cycle. Supported by the data from the power grid [31], the varieties can be defined as $\varphi_{G_0} = 5/8$, $\varphi_{0.4G_0} = 3/8$, respectively.

R_{G_0} and $R_{0.4G_0}$ are given by,

$$R_{G_0} = \frac{\tau^B_{G_0} - \tau^O_{G_0}}{\tau_a} \tag{6}$$

$$R_{0.4G_0} = \frac{\tau^B_{0.4G_0} - \tau^O_{0.4G_0}}{\tau_a} \tag{7}$$

where $\tau^B_{G_0}$ and $\tau^O_{G_0}$ are the output torques of biomimetic blade and original blade in rated condition, respectively ($\tau^O_{G_0} = 2644.48$ N m from simulation), $\tau^B_{0.4G_0}$ is the output torque of biomimetic blade in off-rated condition ($0.4G_0$), $\tau^O_{0.4G_0} = -26.31$ N m, is the output torque of biomimetic blade in off-rated condition ($0.4G_0$), τ_a is the average output torque of the original blade with consideration of proportion for the off-rated operating state, which is given by,

$$\tau_a = \varphi_{G_0} \bullet \tau^O_{G_0} + \varphi_{0.4G_0} \bullet \tau^O_{0.4G_0} \tag{8}$$

Table 6 shows the simulation results of output torque and R_A for the blades with varied A. With A increasing, the output torque kept decreasing in rated condition but that kept increasing in off-rated condition. The comprehensive influence had a peak value when A equaled to 3.15% C_l, indicating that the positive influence of bumpy structure in off-rated condition cannot cover the lost in rated condition when the amplitude was too high. In the end, we chose $A = 3.15\%C_l$ as the optimum level. For the other parameters, downstream width W_D and deflection angle δ varied more widely than others, so we further optimized them by calculating $\tau^B_{0.4G_0}$ for W_D ranging from 3 to 7, and δ ranging from −10 to 30 in the off-rated condition. Table 7 shows the data of calculation results. With the increasing W_D, the output torque decreased first and then ramped up slowly. As the increasing rate of output torque $\tau^B_{0.4G_0}$ was small when W_D was larger than 6% C_P, we determined $W_D = 3\%$ C_P for the final design of bumps on blade. For the optimization of δ, $\tau^B_{0.4G_0}$ reached the peak when $\delta = 10°$. Thus, for the biomimetic bumps on steam turbine blade, the optimal geometrical parameters obtained by orthogonal method and 3-steps optimization were $A = 3.15\%$ C_l, $W_U = 4\%$ C_P, $W_D = 3\%$ C_P, $\delta = 10°$ and $N = 6$. Fig. 11 shows the pressure contours for the original and optimal biomimetic blades. From the simulation results, τ of the optimized biomimetic blade increased from −26.31 N m to 2.13 N m compared with the original blade in the off-rated operating condition. The data suggested that the biomimetic bumps effectively avoided the blade doing work upon the steam flow and enhance the aerodynamic performance in the condition of low mass flow rate.

Meanwhile, this biomimetic structure will shorten the flow passage around bumps. To discuss possible shocks and phase change phenomena in rotor passage, we plot the Mach number contour on the blade height plane that crosses the peak of the third bump, shown in Fig. 12.

From Fig. 12, it can be seen that there was a peak value Mach number ($0.76Ma$) at the pressure side of both for the original blade and biomimetic blade. Although there was another peak value of Mach number ($0.78Ma$) on the suction side for the biomimetic blade, the influence of this peak Mach number was limited around the suction side. The steam flow in rotor passage was still subsonic flow, not producing shocks. However, the relative large Mach number at the suction side did let the local condensation changed. Fig. 13 & 14 show the nucleation rate and liquid volume fraction in the same plane as the Mach number. The steam condensation was concentrated in the upstream of bumps, where the nucleation rate was obviously higher than other positions. Reflected in the liquid volume fraction, there was a liquid concentration in the upstream of bumps. Also, affected by the streamwise vortices, the Mach number and nucleation rate were low in the downstream of bumps. The liquid volume fraction downstream the bumps presented a lower value than that in original blade until the trailing edge. This even made the average dryness in rotor passage of biomimetic blade (0.8885) a bit

Table 6
Effect of amplitude A on R_A.

A (% C_l)	2.80	3.15	3.50	3.85
$\tau^B_{0.4G_0}$ (N•m)	−8.26	−4.91	−2.95	−0.85
$\tau^B_{1.0G_0}$ (N•m)	2631.04	2629.37	2623.47	2619.30
R_A (%)	−0.099	−0.086	−0.266	−0.377

Table 7
Effect of downstream width W_D and deflection angle δ on the output torque.

W_D (% C_P)	3	4	5	6	7
$\tau^B_{0.4G_0}$ (N•m)	1.54	−6.72	−4.91	−1.13	−0.66
δ (°)	−10	0	10	20	30
$\tau^B_{0.4G_0}$ (N•m)	0.31	1.54	2.13	1.84	1.33

higher than that of original blade (0.8880).

3.3. Mechanism of enhanced output torque by bumps

To explore the underlying physics of enhanced output torque, we analyzed the mechanism of the bumpy structures on the evolution of vortex. We characterized the vorticity (Ω) to measure the intensity of vortex,

$$\Omega = \frac{\partial u}{\partial y} - \frac{\partial v}{\partial x} \tag{9}$$

where x and y represent the circumferential and radial direction, respectively, u and v represent the component of steam velocity in x and y direction, respectively.

Fig. 15 shows the mean vorticity of vortices on a downstream plane, which was perpendicular to the suction side. The planes were defined with different distance to bumps. The distance to bumps (ΔS) was given as the space between the peaks of bumps to the planes, as shown in Fig. 15. The vorticity of vortices generated behind the tip bumps will be presented to discuss the development characteristic of vortices.

We picked planes from $\Delta S = 5$ mm to $\Delta S = 195$ mm, presenting the variation of mean vorticity behind the bumps (Fig. 16). The curves in Fig. 16 (a) shows that vortex pairs were generated in close vorticity whereas the counterclockwise vortices dissipated faster. To be specific, the vorticity of counterclockwise vortices declined faster than the clockwise ones and remained in a lower vorticity when vorticity became totally stable. When the vortices develop to 35 mm away from bumps, the mean vorticity stopped the sharp drop to decrease slowly. After that, the dissipation of vorticity tended to be weak. Eventually the mean vorticity of vortex pairs remained stably within 10000 s^{-1}. The visualized development progress of vortices generated behind the top bumps was shown in vorticity contours (Fig. 16 b-e). At the early stage, the

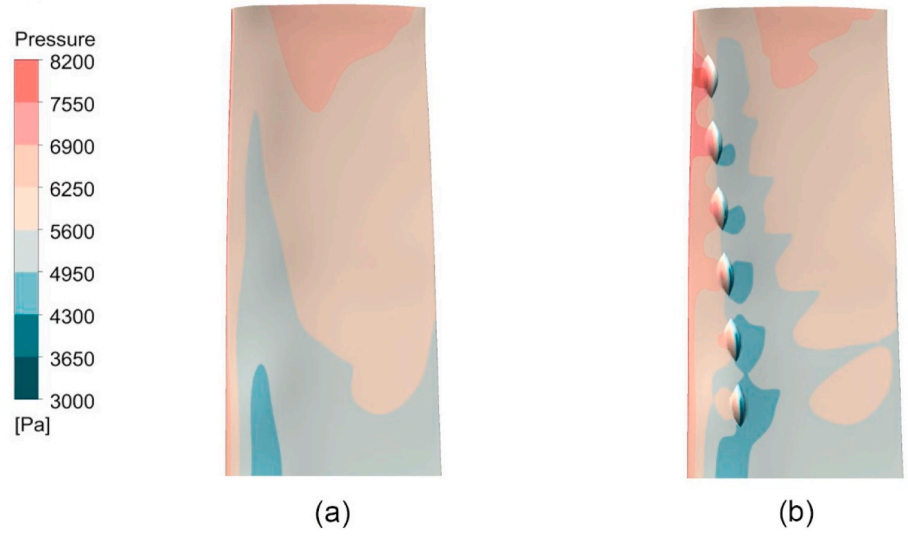

Fig. 11. The pressure distribution on suction side of blade. (a) Original blade. (b) Optimized biomimetic blade.

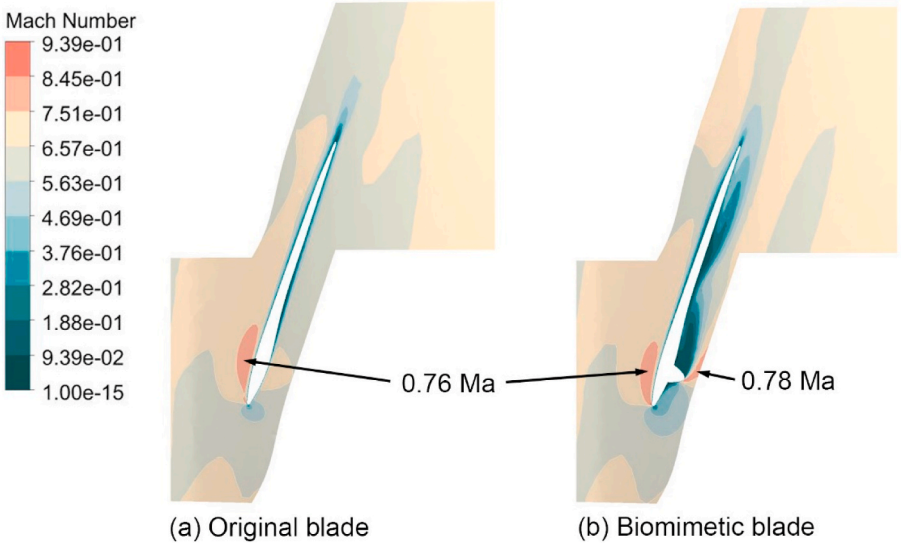

Fig. 12. Comparison of Mach number at the blade height plane (82% l_0).

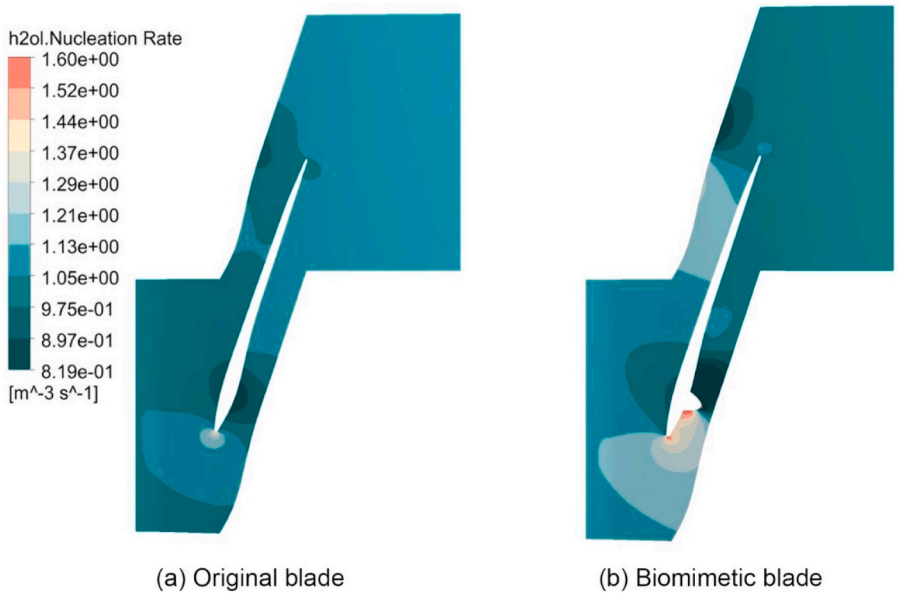

Fig. 13. Comparison of nucleation rate.

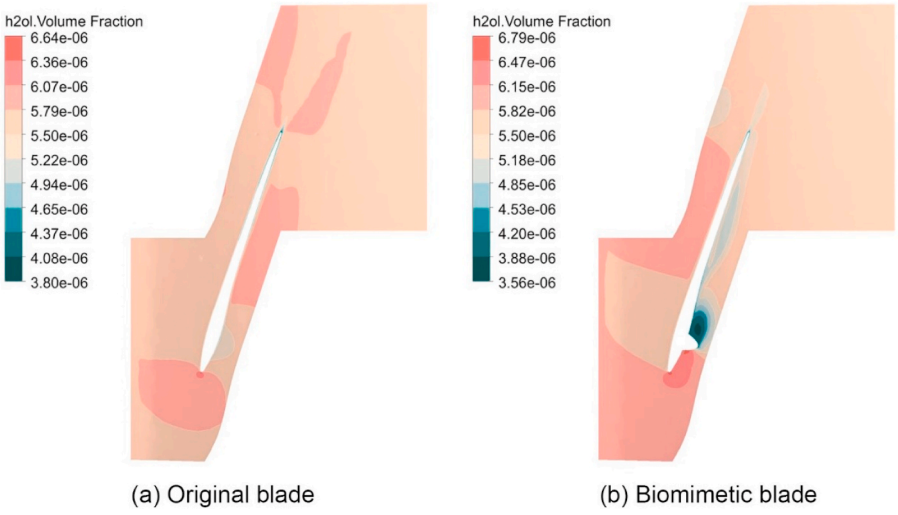

Fig. 14. Comparison of volume fraction of liquid phase.

vortex pair presented in a shape of flat-oval because they were shaped by the bump (Fig. 16 b). Between the vortex pair and the blade surface, there existed a small adverse vortex, marked as second vortex. This phenomenon indicated that the vortex pairs remained strong here ($\Delta S =$ 15 mm), because the second vortex was formed by the rotation of main vortices and the free steam around main vortices. When $\Delta S = 35$ mm, as shown in Fig. 16 (c), the vorticity of this vortex pair behind the top bump had not dropt as the mean vorticity, even though the second vortex disappears. This outstanding performance originated from the steam here was dense and not much influenced by the radial velocity. In Fig. 16 (d), the shape of vortex pairs were close to circle but not symmetry. Through the adequate development, the vortices showed a free shape, like circle. However, in this stage, $\Delta S = 105$ mm, the influence of radial velocity appeared, causing the counterclockwise vortex deformed. Such deforming direction pointed to the tip, which was coincident with the direction of radial velocity. When $\Delta S = 195$ mm, the vortex pair was forced to move toward the tip of blade with the sustained effect of the radial velocity (Fig. 16 e). The vortices generated behind the second bump came in the view as well. Simultaneously the counterclockwise vortices almost disappeared whereas the clockwise vortices remained a relative high vorticity. Here the vorticity was weak and if the vortices continued to develop, they can hardly improve the pressure on suction side evidently. During the whole passage between rotating blades, the counterclockwise vortices were inhibited and all the vortices moved toward the tip because of the radial velocity. These were the unique characteristics in steam turbine. If we considered the vortices kept working until their vorticity reduced to a stable value, the mean effective length was 105 mm in streamwise. The average chord length where the bumps were set was 350 mm. Through comparing these two lengths, we can obtain that the optimized biomimetic blade improved the pressure distribution in 30% steam flow passage.

Combining the development regulation of vortices and the pressure distribution on biomimetic blade, we can conclude that the vortices affected the flow field, leading the pressure on blade surface decreased. Next, we will discuss how the flow field affected by the streamwise vortices. We chose two representative points on blade surface, 20 mm right downstream the peak of third bump (point A) and 20 mm right downstream the mid-tough between the third and the forth bump (point

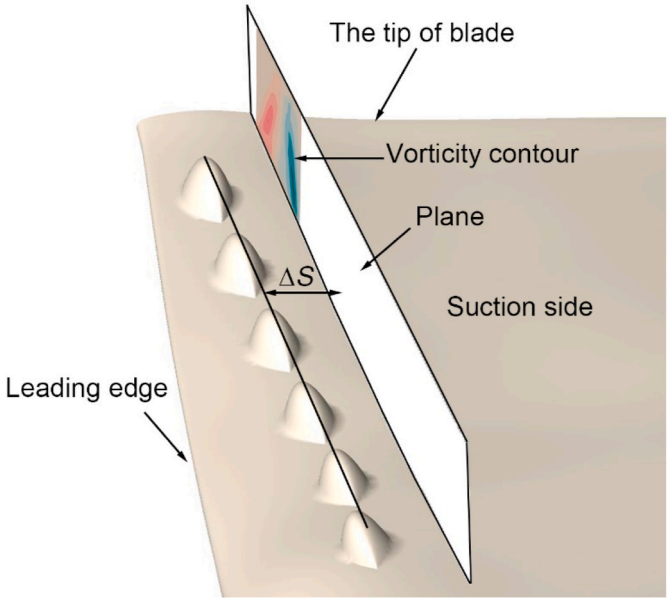

Fig. 15. The distance to bumps (ΔS) was defined as shown. In this section, a series of planes with different ΔS will be created to discuss the variation of vorticity downstream the bumps.

B). Point A was located in the place where the flow field was affected effectively by the streamwise vortices and point B was located in the place where the flow field was little affected. Fig. 17 plots the steam velocity as a function of distance away from the blade surface along the normal direction at point A and B. The curves shows that the thickness of boundary layers at two places are both 5 mm (the length when velocity raises to a stable level). The velocity over point A reached free steam velocity ~300 m/when the distance away from blade was beyond 5 mm. However, influenced by the streamwise vortices, the steam velocity over point A stayed in 50 m/s until ~16 mm away from the blade surface. The velocity reached the same level as the free stream velocity in the distance of 30 mm. The low velocity near the blade inhibited the momentum kinetic energy exchange to the free stream, creating the region with low-pressure on suction side. In short, the vortex weakened the energy exchange between free stream and the suction side to improve the output torque.

3.4. Comparison of bump and vortex generator (VG)

We knew that biomimetic bumps made positive influence to flow field through generating streamwise vortices. In traditional application of industry, the vortex generators, called VGs, were usually used to create vortices. It was useful to discuss the discrepancy of performance between the traditional VGs and the biomimetic bumps. To analyze this, a blade with twelve VGs was built, covering close region the bumps located in. The height (H) of VGs was 0.66 times of boundary layer thickness [32] and the other parameters were set as Pearcey [33] tested, distance between two vanes (D) = 10H, of length of vanes (l) = 3H, mean distance between two vanes (d) = D/4, thickness of vanes (σ) = 1 mm and angle between vanes = 30°, as show in Fig. 18 (a). These values were the suggested optimized ones for parameters of VGs.

We simulated the flow field of blade with VGs in $0.4G_0$ condition and

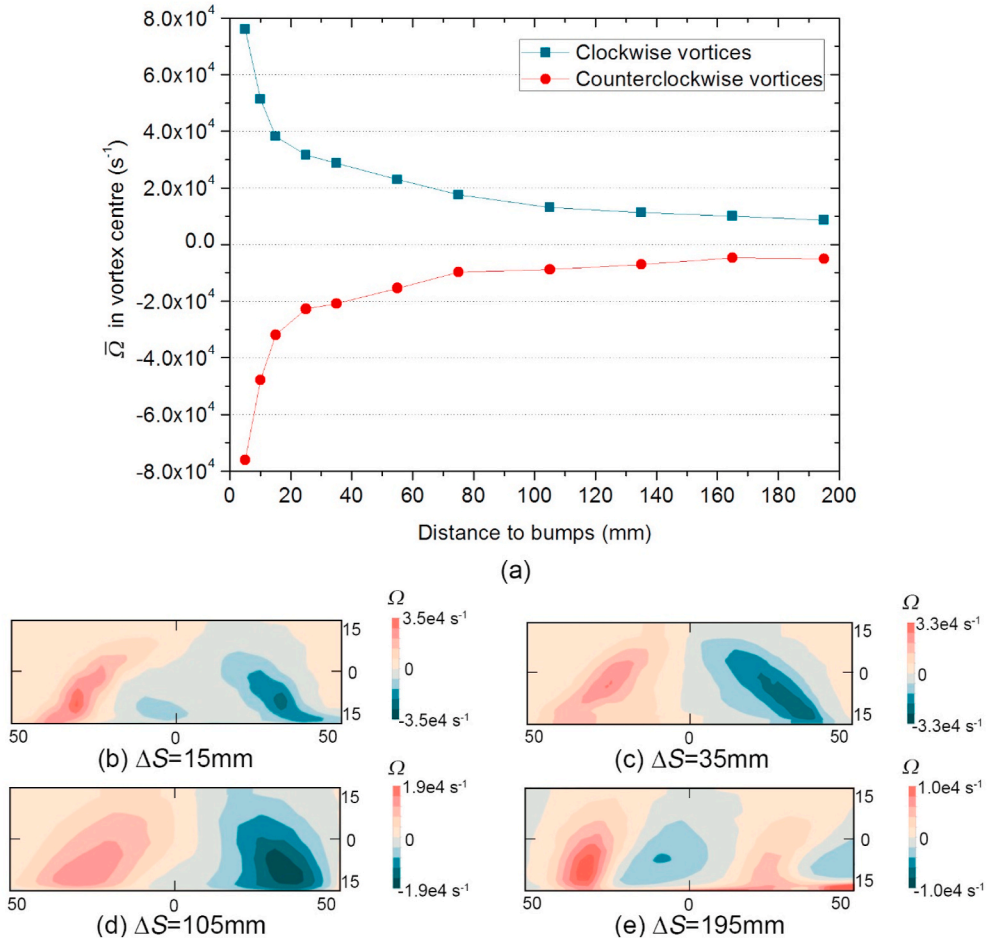

Fig. 16. Vorticity variation of streamwise vortices. (a) Mean vorticity of all vortices behind the bumps. With the vortices develop downstream, the mean vorticity dropt in a sharp decline first and gradually stabilized at around 1×10^4 s^{-1}. The vortices generated behind the top bump were visualized in the distance of 15 mm, 35 mm, 105 mm and 195 mm. (b) At the early stage, the vortices were generated in pairs and in a shape of flat-oval. There existed a small adverse vortex between the vortex pair and blade surface. (c) With the development, the vorticity of vortices decreased and the small vortex disappears. (d) At this stable stage, the vorticity changes less and with adequate development the shape of vortices became round. (e) Influenced by the radial velocity, the counterclockwise vortex was inhibited. The position of vortices was moved toward the tip.

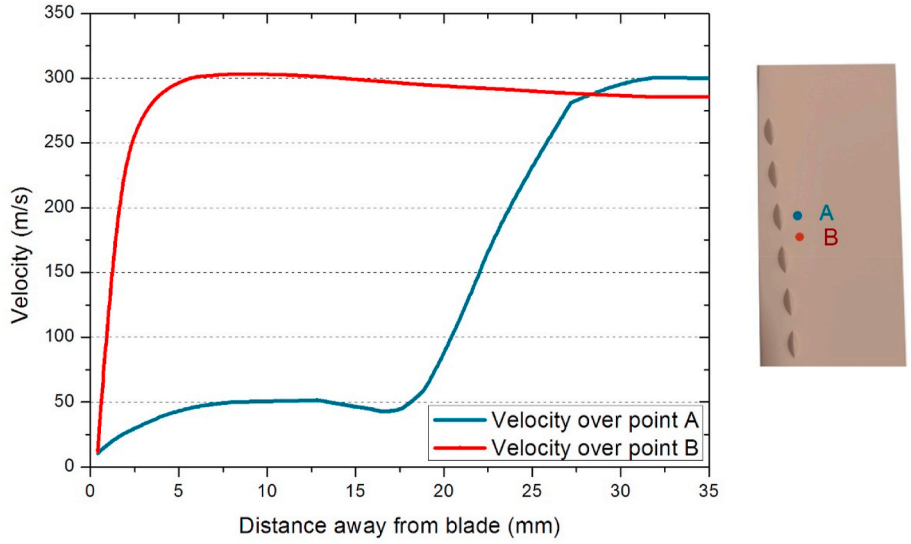

Fig. 17. Velocity of the steam change along the normal direction.

presented the vorticity of streamwise vortices generated by VGs and bumps for comparison. The vorticity contours were shown in Fig. 19. The distances to bumps (ΔS) was the same as that in Fig. 15. Contrasted to the vortices generated by bumps, these vortices had similar max vorticity and developed neatly. The shape of vortices was always approximately circular, not evolving from the shape of flat-oval. The disadvantage lied in the effected region. The size of vortices generated by VGs were small compared with those generated by bumps. The vortices generated by bumps also showed strong and consistent vorticity but those of VGs were weak near the tip side (Fig. 19 (a) and (b)). When $\Delta S = 105$ mm (Fig. 19 (c) and (d)), the vorticity here generated by two structures dropt to a similar level. For the influence of radial velocity became serious in the region close to the root, the vortices there moved toward the tip as the direction of radial velocity. The vorticity of vortices on the biomimetic blade decreased gradually from the tip to the root whereas that on the blade with VGs increased first and decreased. Such distribution caused the vortices generated by VGs to lose the advantage on inhibit the energy exchange, because the flow was denser near the tip side.

Fig. 20 shows the pressure distribution of original blade, biomimetic blade and blade with VGs. Compared to the bumps, the VGs did not created the upstream high pressure region whatever near the tip or not. However, its disadvantage was also obvious that the expansion of low pressure region downstream the structure was less. The VGs mainly effected the pressure distribution around them. When developing to the middle portion of passage, the pressure had few difference from the original blade. Reflected in the output torque, the blade with VGs provided −10.51 N m, remaining a negative value.

Besides, noticed that the modification geometry may bring extra loss in the passage, we defined the total pressure loss coefficient (η) to measure the loss in the passage,

$$\eta = \frac{p_{in}^* - p_{out}^*}{p_{out}^* - p_{out}} \tag{10}$$

where p_{in}^* is the total pressure at inlet, p_{out}^* is the total pressure at outlet, and p_{out} is the static pressure at outlet.

The biomimetic blade brought η of 1.556 and the VGs blade brought η of 2.552. The bumps brought less loss because of the smooth geometry. The VGs were consisted with right angle and flat surface, causing larger loss in the passage. We also simulated the performance of two blades in G_0 and the results showed that τ of VGs blade was 2638.67 N m (0.2% less than the original blade) and τ of biomimetic blade was 2635.32 N m (0.3% less than the original blade). This indicated that the modification hardly affected performance of rated condition. The optimum biomimetic blade enhanced the output torque with low pressure loss and had little impact on the blade performance in rated condition.

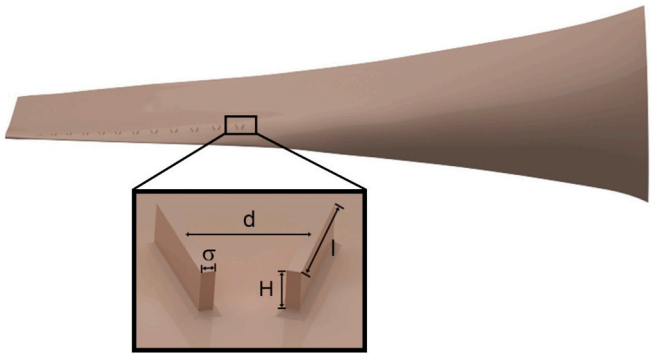

Fig. 18. Twelve VGs were mounted along the region with low-pressure. The parameters VG were controlled by local thickness of boundary layer except the vane thickness which equaled 1 mm. The height of VGs (H) was 0.66 times of local thickness of boundary layer. The length of vanes (l) equaled 3H. The distance between two vanes (D) equaled 10H and the mean distance between two vanes (d) equaled D/4.

4. Conclusions

In this work, we designed a new LP last stage blade of steam turbine with biomimetic bumps for raising the aerodynamic performance in low mass flow condition. We mainly discussed the function of biomimetic blade in $0.4G_0$ condition. The biomimetic bump was defined by five parameters, amplitude, wavelength, upstream width, downstream width and deflection angle. The simulation results showed that the bumps generated streamwise vortices. Through analyzing the blade profile, we noticed that setting bumps on the low pressure region of suction side can guarantee the generation and development of streamwise vortices. The result showed that no shocks appeared around the bumps when Mach number changed there. The bumps also had little influence on cascade dryness. In this way, the biomimetic blade brought rise on the output torque (from −26.31 N m to −15.99 N m). By the orthogonal analysis and refinement, the parameters of the bump were optimized. The output torque of optimum biomimetic blade reached 2.13 N•m, enhanced from a negative value to a positive value. We further studied the mechanism of the bump. The vortices generated by

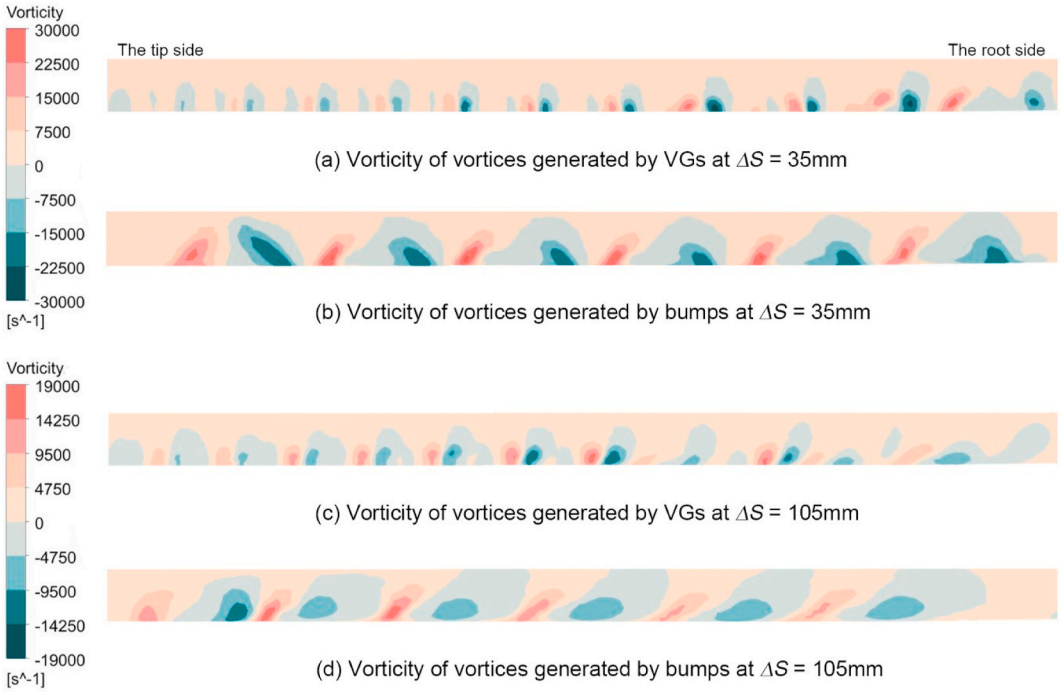

Fig. 19. Vorticity of vortices. (a) Vortices were generated by VGs at $\Delta S = 35$ m. (b) Vortices were generated by bumps at $\Delta S = 35$ m. (c) Vortices were generated by VGs at $\Delta S = 105$ m. (d) Vortices were generated by bumps at $\Delta S = 105$ m.

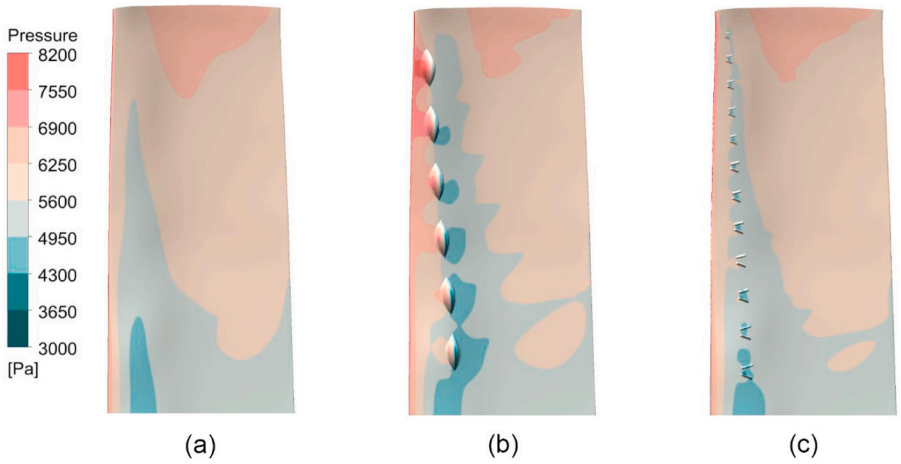

Fig. 20. The pressure distribution on suction side of blade. (a) Original blade and $\tau = -26.31$ N m. (b) Biomimetic blade and $\tau = 2.13$ N m. (c) Blade with VGs and $\tau = -10.51$ N m.

bumps remained effective vorticity over at least 30% of the passage. In this portion, the vortices forced the blade surface to exchange energy with the low velocity flow, effectively reducing the applied pressure by the free steam. Through the widely influence from streamwise vortices, the output torque of biomimetic blade was enhanced. Since the core function of bumps was generating vortices. We also explored the discrepancy of bumps and vortex generators (VGs). Both blades hardly affected the aerodynamic performance in rated condition. Compared to the blade with VGs, the biomimetic blade created a smooth flow passageway. The pressure loss of biomimetic blade was 40% less than that of the blade with VGs while the output torque was 120% that of the blade with VGs. This design can effectively enhance the aerodynamic performance of turbine blade in low mass flow condition and cause little loss in rated condition.

Declaration of competing interest

The authors declare that they have no known competing financial interests or personal relationships that could have appeared to influence the work reported in this paper.

Data availability

Data will be made available on request.

Acknowledgements

The financial support of this paper was provided by the National Natural Science Foundation of China (Grant No. 51776142).

Nomenclature

AOA	Angle-of-attack (°)
VG	Vortex generator
τ	Output torque
l_0	Height of blade (mm)
C_l	Axial chord length of blade (mm)
A	Amplitude of bump
N	Number of bump
W_U	Upstream width of bump
W_D	Downstream width of bump
δ	Deflection angle of bump (°)
P_c	Bump position in chordwise
P_l	Bump position in radial wise
C_p	Length of suction side profile (mm)
χ	Mass fraction of the vapor
h_{mix}	Mixture static enthalpy (J kg^{-1})
$h_{sat,l}(p)$	Saturation enthalpy of liquid (J kg^{-1})
$h_{sat,v}(p)$	Saturation enthalpy of vapor (J kg^{-1})
ψ	Thermophysical property of fluid
ρ_{mix}	Density of liquid-vapor mixture (kg m^{-3})
$\rho_{sat,l}$	Density of saturated liquid (kg m^{-3})
$\rho_{sat,v}$	Density of saturated vapor (kg m^{-3})
G_0	Mass flow rate in rated condition (kg s^{-1})
$\overline{\tau}$	Average output torque in orthogonal design (N•m)
S	Blade surface (m)
$\widehat{\tau}$	Stress tensor on a micro-surface of blade
$\overrightarrow{n}$	unit normal vector of the micro-surface
$\overrightarrow{r}$	position vector
$\overrightarrow{z}$	unit vector of axis
R_A	Characteristic parameter for judging performance of bump
R_{G_0}	Ramp of output torque in the rated condition
$R_{0.4G_0}$	Ramp of output torque in the off-rated condition
φ_{G_0}	Time coefficient for the rated condition
$\varphi_{0.4G_0}$	Time coefficient for the off-rated condition
τ_a	Average output torque of original blade in a power grid cycle (N•m)
$\tau^B_{G_0}$	Output torques of biomimetic blade in rated condition (N•m)
$\tau^O_{G_0}$	Output torques of original blade in rated condition (N•m)
$\tau^B_{0.4G_0}$	Output torques of biomimetic blade in off-rated condition (N•m)
$\tau^O_{0.4G_0}$	Output torques of original blade in off-rated condition (N•m)
Ω	Vorticity of streamwise vortex (s^{-1})
ΔS	Distance to bumps (mm)
H	Height of vortex generator (mm)
D	Distance between two vanes (mm)
l	Length of vanes (mm)
d	Mean distance between two vanes (mm)
σ	Thickness of vanes (mm)
η	Total pressure loss coefficient
p	Total pressure (kPa)

References

[1] Z. Fang, C. Gong, A. Revell, G. Chen, A. Harwood, J. O'Connor, Passive separation control of a NACA0012 airfoil via a flexible flap, Phys. Fluids (2019) 31.

[2] D. Hoseinzade, E. Lakzian, S. Dykas, Optimization of the Trailing Edge Inclination of Wet Steam Turbine Stator Blade towards the Losses Reduction, Experimental Techniques, 2022.

[3] Z. Han, W. Zeng, X. Han, P. Xiang, Investigating the dehumidification characteristics of turbine stator cascades with parallel channels, Energies (2018) 11.

[4] S. Huang, Y. Hu, Y. Wang, Research on Aerodynamic Performance of a Novel Dolphin Head-Shaped Bionic Airfoil, Energy, 2021.

[5] G. Bampanis, M. Roger, S. Moreau, Chiciudfan, on a three-dimensional investigation of airfoil turbulence-impingement noise and its reduction by leading-edge tubercles, J. Sound Vib. (2022) 520.

[6] F.E. Fish, G.V. L, Passive and active flow control by swimming fishes and mammals, Annu. Rev. Fluid Mech. 38 (2006) 193–224.

[7] L.N. Cooper, A. Berta, S.D. Dawson, J.S. Reidenberg, Evolution of hyperphalangy and digit reduction in the cetacean manus, Anat. Rec. 290 (2007) 654–672.

[8] F.E. Fish, P.W. W, M.M. Murray, L.E. Howle, The tubercles on humpback whales' flippers: application of bio-inspired technology, Integr. Comp. Biol. 51 (2011) 203–213.

[9] E.A. van Nierop, S. Alben, M.P. Brenner, How bumps on whale flippers delay stall: an aerodynamic model, Phys. Rev. Lett. 100 (2008).

[10] H. T. C. Pedro, M. H. Kobayashi, Numerical Study of stall delay on humpback whale flippers. 46th AIAA Aerospace Sciences Meeting and Exhibit, 7-10 January 2008, Reno, Nevada.

[11] A. Corsini, , G. D, A.G. Sheard, On the role of leading edge bumps in the control of stall onset in axial fan blades, J. Fluids Eng. -Trans. ASME 135 (2013).

[12] Z. Carija1, , E. M, Z. Novak, S. Fućak, Numerical analysis of aerodynamic characteristics of A bumped leading edge turbine blade, Eng. Rev. 34 (2) (2014) 93–101.

[13] C.J. Bai, W. Wang, P.W. Chen, The effects of sinusoidal leading edge of turbine blades on the power coefficient of horizontal-axis wind turbine (HAWT), Int. J. Green Energy 13 (2016) 1193–1200.
[14] W.A. Shi, N. Mehmet, A. Rosemary, T. Batuhan, Serkan, Numerical optimization and experimental validation for a tidal turbine blade with leading edge tubercles, Renew. Energy 96 (2016) 42–55.
[15] K.L. Hansen, N. Rostamzadeh, R.M. Kelso, B.B. Dally, Evolution of the streamwise vortices generated between leading edge tubercles, J. Fluid Mech. 788 (2016) 730–766.
[16] H. Johari, C. Henoch, D. Custodio, A. Levshin, Effects of leading edge protuberances on airfoil performance, AIAA J. 45 (2007) 2634–2642.
[17] Cai Chang, Shuhong Liu, Zhigang Zou, Takao Maeda, Yasunari Kamada, Qing'an Li, Ryota Sato, Experimental and theoretical investigations on the effect of a single leading-edge protuberance on airfoil performance, Phys. Fluids (2019) 31.
[18] H.S. Yoon, P.A. Hung, J.H. Jung, M.C. Kim, Effect of the wavy leading edge on hydrodynamic characteristics for flow around low aspect ratio wing, Comput. Fluid 49 (2011) 276–289.
[19] J. Favier, A. Pinelli, U. Piomelli, Control of the separated flow around an airfoil using a wavy leading edge inspired by humpback whale flippers, Compt. Rendus Mec. 340 (2012) 107–114.
[20] P.W. Weber, L.E. Howle, M.M. Murray, D.S. Miklosivic, Computational evaluation of the performance of lifting surfaces with leading edge protuberances, J. Aircraft 48 (2011).
[21] H. Arai, Y. Dio, T. Nakashima, H. Mutsuda, A study on stall delay by various wavy leading edges, J. Aero Aqua Bio-Mech. 1 (2010) 18–23.
[22] Y. Zhang, Z. Guo, X. Zhu, Y. Li, X. Song, C. Cai, Y. Kamada, T. Maeda, Q. Li, Investigation of Aerodynamic Forces and Flow Field of an H-type Vertical axis Wind Turbine Based on Bionic Airfoil, Energy, 2022, p. 242.
[23] D. Serson, J.R. Meneghini, S.J. Sherwin, Derect numerical simulations of the flow around wings with spanwise waviness, J. Fluid Mech. 826 (2017) 714–731.
[24] N. Rostamzadeh, R.M. Kelso, B. Dally, A numerical investigation into the effects of Reynolds number on the flow mechanism induced by a tubercled leading edge, Theor. Comput. Fluid Dynam. 31 (2017) 1–32.
[25] F. Wu, D. Xie, J. Zhang, H. Zhang, C. Wang, Improvement of steam turbine blade foil with biomimetic design and its influence on aerodynamic performance, in: ASME Turbo Expo 2019: Turbomachinery Technical Conference and Exposition, GT, 2019. Proceedings of the ASME Turbo Expo, vols. 8, 2019.
[26] J. Michalek, M. Monaldi, T. Arts, Aerodynamic performance of a very high lift low pressure turbine airfoil (T106C) at low Reynolds and high Mach number with effect of free stream turbulence intensity, J. Turbomach. 134 (2012).
[27] N. Herzog, M. Binner, J.R. Seume, K. Rothe, Verification of low-flow conditions in a multistage turbine, Proc. ASME Turbo Expo 6 (2007) (Pts A and B).
[28] Uicker J., Tohme B., Bergmann D., Stannowski G., Windage effect on HP sections of reheat steam turbines. Int. Joint Power Gener. Conf., Vol. 10.
[29] A. Mambro, F. Conglu, E. Gallonl, Influence of the snubber on temperature distribution at last stage blade exit of a steam turbine during low volume flow operations, Appl. Therm. Eng. (2019) 937–952.
[30] S. Dykas, M. Majkut, M. Strozik, K. Smolka, Experimental study of condensing steam flow in nozzles and linear blade cascade, Int. J. Heat Mass Tran. (2015) 50–57.
[31] S. Jianjian, C. Chuntian, L.I. Weidong, et al., Solutions to power generation allocation among multiple power grids in peak operation of hydro, thermal and nuclear plants, Proc. CSEE 34 (2014) 1041–1051.
[32] J.C. Lin, Review of research on low-profile vortex generators to control boundary-layer separation, Prog. Aero. Sci. 38 (4) (2002) 389–420.
[33] H.H. Pearcey, Boundary layer and flow control, its principles and applications, in: G.V. Lachmann (Ed.), Part 4: Shock-Induced Separation and its Prevention by Design and Boundary Layer Control, Pergamon, Oxford, 1961.